Analytical and numerical modeling of viscous anisotropy: A toolset to constrain the role of mechanical anisotropy for regional tectonics and fault loading.

Dunyu Liu[1], Simone Puel[1,2], Thorsten W. Becker[1,2,3], Louis Moresi[4]

[1]Institute for Geophysics, Jackson School of Geosciences, The University of Texas at Austin

[2]Department of Geological Sciences, Jackson School of Geosciences, The University of Texas at Austin

[3]Oden Institute for Computational Engineering and Sciences, The University of Texas at Austin

[4]Research School of Earth Science, Australian National University, Canberra, Australia

This manuscript is a preprint uploaded to *EarthArXiv*. This preprint has been submitted for publication in *Geophysical Journal International* and has not yet been peer-reviewed. We welcome feedback, discussion, and comments at any time. Feel free to get in touch with the authors.

Corresponding author: Dunyu Liu

Email: dliu@ig.utexas.edu

Highlights:

- Mechanical anisotropy causes stress heterogeneity and non-coaxiality of principal stress and strain rates
- An analytical solution for a viscously anisotropic layer under shear is derived
- *FEniCS* based finite element code is developed for more complicated scenarios
- An approach to evaluate mechanical viscous anisotropy from observations is suggested

Abstract

Whether mechanical anisotropy is required to explain the dynamics of the lithosphere, in particular near fault zones where it may affect loading stresses, is an important yet open question. If anisotropy affects deformation, how can we quantify its role from observations? Here, we derive analytical solutions and build a theoretical framework to explore how a shear zone with anisotropic viscosity can lead to deviatoric stress heterogeneity as well as non-coaxial principal stress and strain rates. We also develop an open-source finite element approach to explore more complex scenarios in both 2-D and 3-D, and simulate three 3-D scenarios inspired by an anisotropic major strike-slip fault zone, the asthenospheric mantle, and the Leech River Schist above the Cascadia subduction zone. Our findings and new tools may help geoscientists to better understand, detect, and evaluate mechanical anisotropy in natural settings, with potential implications including the transfer of lithospheric stress and deformation including fault loading.

1 Introduction

Mechanical anisotropy can refer to either elastic moduli or creep viscosities depending on the style and orientation of deformation. The former is important for seismic wave propagation, but in particular the viscous, long-term deformation type of mechanical anisotropy is important for geodynamic processes (e.g. Vauchez *et al.*, 1998). Viscous anisotropy of the crust and lithospheric mantle might be caused by the effects of melt (e.g., Takei and Katz, 2013), embedded structural zones of weakness (shape preferred orientation, SPO; e.g., Montési, 2013), or may be due to crystallographically preferred orientations (CPOs) of intrinsically anisotropic olivine crystals (e.g. Tommasi *et al.*, 2009). The resulting mechanical anisotropy can be preserved at lithospheric scale, i.e., tectonic inheritance (Vauchez *et al.*, 1998), or concentrated into narrow shear zones within the lithosphere, where spatial variations in viscous anisotropy result in strain localization in plate interiors that may affect flexural strength (e.g., Simons and van der Hilst, 2003) or intraplate seismicity (Mameri *et al.*, 2021).

Olivine-aggregate deformation experiments show textures with significant viscous anisotropy (e.g., Hansen *et al.*, 2016). Mechanical anisotropy is thus expected as a result of CPOs, and the development of the latter is explored widely in the context of connecting mantle flow and seismic anisotropy (e.g. Long and Becker, 2010; Becker and Lebedev, 2021). Any feedback between mechanical anisotropy and convection may then affect the predictions for seismic anisotropy, for example. However, at least within an instantaneous flow scenario, mechanical anisotropy is hard to distinguish from isotropic weakening (Becker and Kawakatsu, 2011). Time-dependent scenarios of deformation may be more affected by mechanical anisotropy (Christensen, 1987; Mühlhaus *et al.*, 2004; Király *et al.*, 2020; Lev and Hager, 2011; Perry-Houts and Karlstrom, 2019) compared to an isotropic asthenosphere.

It is thus important to further constrain the role of mechanical anisotropy for the lithosphere, and observations from tectonically well constrained regional settings provide an opportunity to explore complementary strain and stress sensitive data (e.g., Mameri *et al.*, 2021). In turn, mechanical anisotropy may affect some of the methods used to infer stress or stressing rate close to faults, such as inversion of focal mechanisms (e.g. Kaven *et al.*, 2011). In Southern California, for example, inherited CPOs and alignment of weak layers through SPO could both be a source of mechanical anisotropy, and the reactivation of preexisting fault structures may affect the tectonic plate motion deformation response and local fault loading (Schulte-Pelkum *et al.*, 2021 and references therein). Studies that explore the effects of mechanical anisotropy on regional scales for Southern California are, however, still limited.

Ghosh *et al.* (2013) implemented an anisotropic San Andreas Fault (SAF) in a 3-D global model but failed to identify robust indicators of mechanical anisotropy on regional scales. However, if mechanical anisotropy is considered in a regional scale model, it may be easier to assess the documented non-coaxiality between stress and strain (Schulte-Pelkum *et al.*, 2021), and to eventually incorporate time dependence in a field observation validated way. This suggests an opportunity to develop new methods for inferring mechanical anisotropy from field observations and further constrain fault loading.

In this study, we work toward a theoretical framework and first solve analytically the deformation of a simple 2-D model with a viscously anisotropic layer. The solution shows stress heterogeneity and non-coaxial principal stress and strain rates inside the anisotropic layer and reveals the mechanics behind such heterogeneity. Second, we explore how the orientation and strength of the mechanical anisotropy affect the non-coaxiality and stress heterogeneity. Third, we present a new, open-source finite-element tool, its validation against the analytic solution, and applications to three 3-D scenarios. Lastly, we discuss the implications and potential applications of the method and tools.

2 The analytic solution of a 2-D layered model with viscous anisotropy

Motivated by not necessarily intuitive solutions produced by numerical tests, e.g. based on our earlier implementations (Moresi *et al.*, 2003, Becker and Kawakatsu, 2011), we proceed to solve the incompressible Stokes flow equation for a 2-D layered model that is subjected to simple shearing, where a central viscously anisotropic layer is sandwiched between two isotropic layers (Figure 1). The mathematical formulation of viscous anisotropy follows Moresi and Mühlhaus (2006) with $\boldsymbol{n}$ the "director" of the weak viscous direction. The boundary conditions are 1) horizontal velocity on the top, 2) fixed velocity at the bottom, and 3) periodic on the two lateral boundaries.

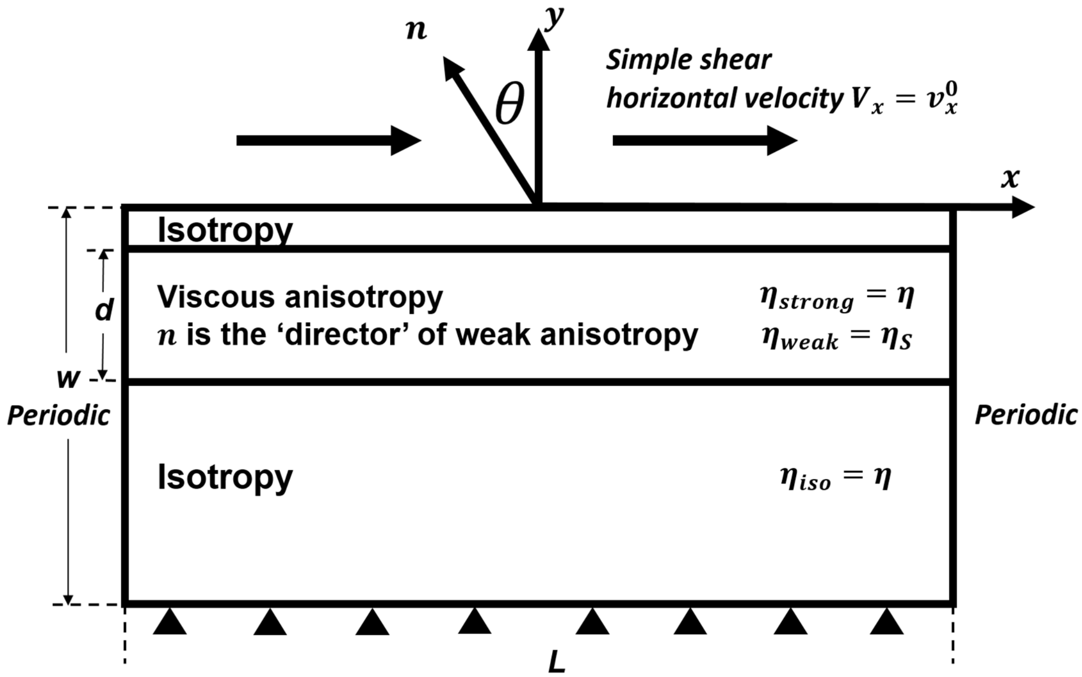

Figure 1. Schematic of the 2-D layered model with a middle viscously anisotropic layer subjected to simple shearing. $\boldsymbol{n}$ is the "director" of weak viscous (η_{weak}) direction. The viscosity of the strong direction in the anisotropic layer and the isotropic viscosity are η_{strong} and η_{iso}, respectively. The model domain is L by w with the anisotropic layer with a width of d. θ is the angle from y axis to $\boldsymbol{n}$. The bottom of the model is fixed with zero velocity. The top of the model shears horizontally with a velocity of v_x^0. Velocity and pressure on the left and right lateral boundaries are periodic.

The mathematical description of the boundary-value problem is expressed in eq. (1).

$$\begin{cases} -\boldsymbol{\nabla} \cdot (\boldsymbol{\sigma} + p) = \boldsymbol{f} & in\ \Omega \\ \boldsymbol{\nabla} \cdot \boldsymbol{v} = 0 & in\ \Omega \\ \mathbf{D} = (\nabla \boldsymbol{v} + \nabla \boldsymbol{v}^{\mathrm{T}})/2 & in\ \Omega \\ \boldsymbol{\sigma} = 2\eta \mathbf{D} & in\ \Omega_{iso} \\ \boldsymbol{\sigma} = 2\eta \mathbf{D} - 2(\eta - \eta_S)\boldsymbol{\Lambda} : \mathbf{D} & in\ \Omega_{aniso} \\ v_x = v_x^0 & on\ \Gamma_D|_{y=0} \\ v_x = 0, v_y = 0 & on\ \Gamma_D|_{y=-w} \\ periodic\ v & on\ \Gamma_D|_{x=\pm L/2} \end{cases} \quad (1)$$

where Ω, Ω_{iso}, Ω_{aniso} are domains of the whole model, the isotropic region, and the anisotropic region, respectively. Γ_D is the Dirichlet boundary of the domain Ω. $\boldsymbol{\sigma}, p, \boldsymbol{v}$ are stress, pressure, velocity fields. $\boldsymbol{f}$ is the body force, which is assumed to be zero in the following discussion. η is the isotropic viscosity and the strong anisotropic viscosity. η_S is the weak anisotropic viscosity. $\mathbf{D}$ is the 2$^{\mathrm{nd}}$-order strain rate tensor, $\boldsymbol{\Lambda}$ is 4$^{\mathrm{th}}$-order material property matrix for the anisotropic material. $\Lambda_{ijkl} = (\frac{1}{2}\left(n_i n_k \delta_{lj} + n_j n_k \delta_{il} + n_i n_l \delta_{kj} + n_j n_l \delta_{ik}\right) - 2n_i n_j n_k n_l)$ where in 2-D n_i $(i = x, y)$ is the vector of the normal director of weak anisotropic direction (Mühlhaus *et al.*, 2002; Moresi and Mühlhaus, 2006).

Given the symmetry of our model assumptions (e.g., boundary conditions, geometry, model setup),

$$v_y = v_{x,x} = \sigma_{xx,x} = \sigma_{xy,x} = \sigma_{yy,x} = p_{,x} = 0 \quad (2)$$

where for example $v_{x,x}$ stands for ${}^{\partial v_x}/_{\partial x}$.

Substituting eq. (2) into eq. (1), we get

$$D_{xx} = v_{x,x} = 0 \quad \text{(3a)}$$

$$D_{yy} = v_{y,y} = 0 \quad \text{(3b)}$$

$$D_{xy} = \left(v_{x,y} + v_{y,x}\right)/2 = v_{x,y}/2 \quad \text{(3c).}$$

In the isotropic layer, stress components follow

$$\sigma_{xx} = \sigma_{yy} = 0, \sigma_{xy} = \eta v_{x,y} \quad \text{(4).}$$

In the anisotropic layer, after substituting **Λ** and **D** in eq. (1), the stress components read

$$\sigma_{xx} = -2(\eta - \eta_S)\left(n_x n_y - 2n_x^3 n_y\right) v_{x,y} \quad \text{(5a)}$$

$$\sigma_{xy} = \eta v_{x,y} - (\eta - \eta_S)\left(1 - 4n_x^2 n_y^2\right) v_{x,y} \quad \text{(5b)}$$

$$\sigma_{yy} = -2(\eta - \eta_S)\left(n_x n_y - 2n_x n_y^3\right) v_{x,y} \quad \text{(5c).}$$

We assume $v_{x,y}$ to be constants s_1 and s_2 in the isotropic and anisotropic layer, respectively. Then, eq. (4) is converted to

$$\sigma_{xy} = \eta s_1 \text{ (6a)}$$

$$\sigma_{xx} = \sigma_{yy} = 0 \text{ (6b)}$$

while eq. (5) can be written as

$$\sigma_{xx} = -2(\eta - \eta_S)\left(n_x n_y - 2n_x^3 n_y\right) s_2 \text{ (7a)}$$

$$\sigma_{xy} = \eta s_2 - (\eta - \eta_S)\left(1 - 4n_x^2 n_y^2\right) s_2 \text{ (7b)}$$

$$\sigma_{yy} = -2(\eta - \eta_S)\left(n_x n_y - 2n_x n_y^3\right) s_2 \text{ (7c).}$$

The continuity condition for the shear stress σ_{xy} and the normal stress $\sigma_{yy} + p$ on the interfaces between the isotropic and anisotropic layers require

$$\eta s_1 = \eta s_2 - (\eta - \eta_S)(1 - 4n_x^2 n_y^2)s_2 \quad (8)$$

$$p^{iso} = -2(\eta - \eta_S)(n_x n_y - 2n_x n_y^3)s_2 + p^{aniso} \quad (9),$$

where p^{iso} and p^{aniso} are pressures inside the isotropic and anisotropic layers, respectively.

The boundary condition for $v_x(y = 0) = v_x^0$ and $v_x(y = -w) = 0$ and the integration of $v_{x,y}$ over the whole width w can be expressed as

$$\int_{-w}^{0} v_{x,y}\, dy = v_x|^0 - v_x|^{-w} = v_x^0,$$

which gives

$$\int_{-w}^{0} v_{x,y}\, dy = \int_{-d}^{0} s_2\, dy + \int_{-w}^{-d} s_1\, dy = s_2 d + (w - d)s_1,$$

and then

$$s_2 d + (w - d)s_1 = v_x^0 \quad (10).$$

Combining eqs. (8) and (10) we get

$$s_2 = v_x^0 / [w - \left(1 - \frac{\eta_S}{\eta}\right)(1 - 4n_x^2 n_y^2)(w - d)] \text{ (11a)}$$

$$s_1 = (v_x^0 - s_2 d)/(w - d) \text{ (11b)}$$

Substituting s_1 and s_2 back to eqs. (6), (7), and (9), we get solutions for velocities, stresses, and pressure.

2.1 The character of the analytic solution

We calculate a dimensionless case with $w = 1$, $\eta = 1$, $v_x^0 = 1$, and $d = 0.4$ (width between –0.1 and –0.5). We change the director $\boldsymbol{n}$ of the weak viscous direction by varying θ (Figure 1) from 0° to 90°, and the contrast between the strong and weak viscosities $\gamma = \eta/\eta_S$ in the anisotropic layer to explore their effects on stress and strain rate distributions. We increase θ at a step of 2.5° and we first compute the scenario with γ of 10.

Figure 2a shows the maximum principal stress σ_1 (white bars; negative compressive), and maximum principal strain rate $\dot{\varepsilon}_1$ (gray bars; negative compressive), and the maximum shear stress σ_{xy}^{max} (background) on the middle vertical profile between the width –0.45 and –0.65, where sharp changes of the quantities occur, for various values of θ. Principal stress axes inside the anisotropic layer are mismatched relative to the principal strain rate axes, which are always at 45° to the horizontal axis, while the principal stresses align with principal strain rates inside the isotropic layer.

This mismatch occurs for a wide range of θ and the magnitude of mismatch depends on θ and, as shown below, γ. The results are symmetric relative to $\theta = 45°$, therefore we will limit our presentation to θ less than 45°. In addition, maximum shear stress and pressure show heterogeneities across the layer interface, unlike what might be expected from stress continuity for an isotropic medium. Figure 2b and 2c show maximum shear stress and pressure as a function of width for five θ of 2.5, 12.5, 22.5, 32.5, and 42.5°, respectively. The largest stress and pressure heterogeneity occur at θ of 12.5 and 22.5°, respectively.

The mismatch of principal stress and strain rate axes could thus be a potential indicator of viscous anisotropy from field observations (cf. Mameri *et al.*, 2021). Correspondent stress and pressure heterogeneity may significantly influence mechanical processes inside the anisotropic zone, and lead to reinterpretations of the relative crustal stress levels and patterns within faults and their surroundings (e.g., Hardebeck and Michael, 2004, Hirano and Yamashita, 2011).

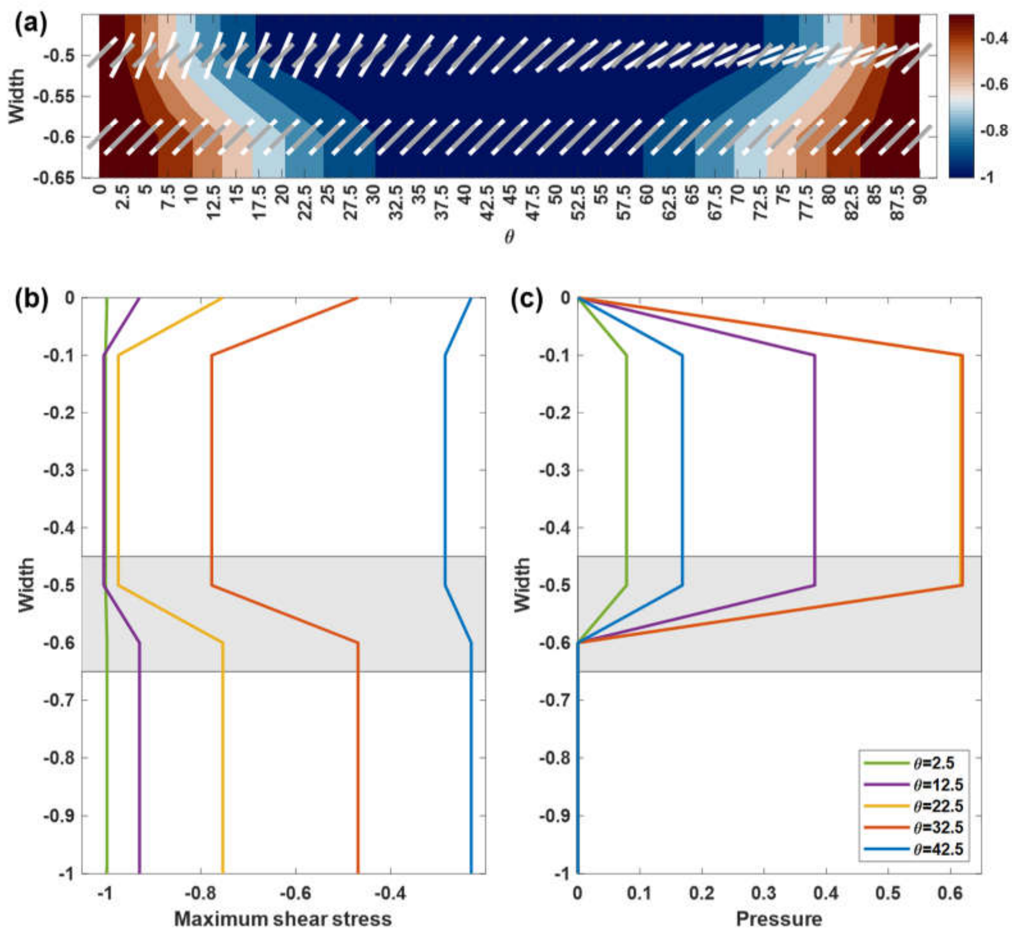

Figure 2. (a) Principal stress σ_1 (white bars), principal strain rate $\dot{\varepsilon}_1$ (gray bars), and

maximum shear stress σ_{xy}^{max}(background map) on the middle vertical profile as a function of θ in the model with viscosity contrast of 10. We only show the model domain near the layer interface between -0.45 to -0.65, where sharp changes of quantities occur. (b) and (c) are maximum shear stress and pressure as a function of width for five θ of 2.5, 12.5, 22.5, 32.5, and 42.5°, respectively. The model domain shown in panel (a) is shaded.

We then calculate scenarios with various $\gamma = \eta/\eta_S$, which affect the magnitudes of the heterogeneity and mismatch. Figure 3a shows the angles between the maximum principal stress σ_1, maximum principal strain rate $\dot{\varepsilon}_1$, and the director $\boldsymbol{n}$ as a function of θ at a central point (x = 0, y = -0.3) inside the anisotropic layer for three values of γ of 2, 10, and 100, respectively. θ_1 and θ_2 are angles between σ_1 and $\boldsymbol{n}$, and between $\dot{\varepsilon}_1$ and $\boldsymbol{n}$, respectively. $\alpha = \theta_1 - \theta_2$ is the angular mismatch between σ_1 and $\dot{\varepsilon}_1$. α is zero when $\theta = 45°$ and starts to increase with decreasing θ until reaches its peak. The peak angular mismatch α for a wider range viscosity contrast γ is shown in Figure 4, where we vary γ from near unity to 10^5. When the viscosity contrast γ increases, the peak of α increases and it occurs at smaller θ. If γ is close to 1, α will approach to zero and the model essentially turns to the isotropic scenario. If γ increases, the mismatch α will increase to the maximum 45° when θ approaches to zero, akin to deformation along the weak anisotropic direction being a stress free boundary. For $\gamma = 10$, perhaps appropriate for olivine CPOs (Hansen *et al.*, 2012), the peak angular mismatch α could be as large as about 27.45° when $\theta = 8.8°$.

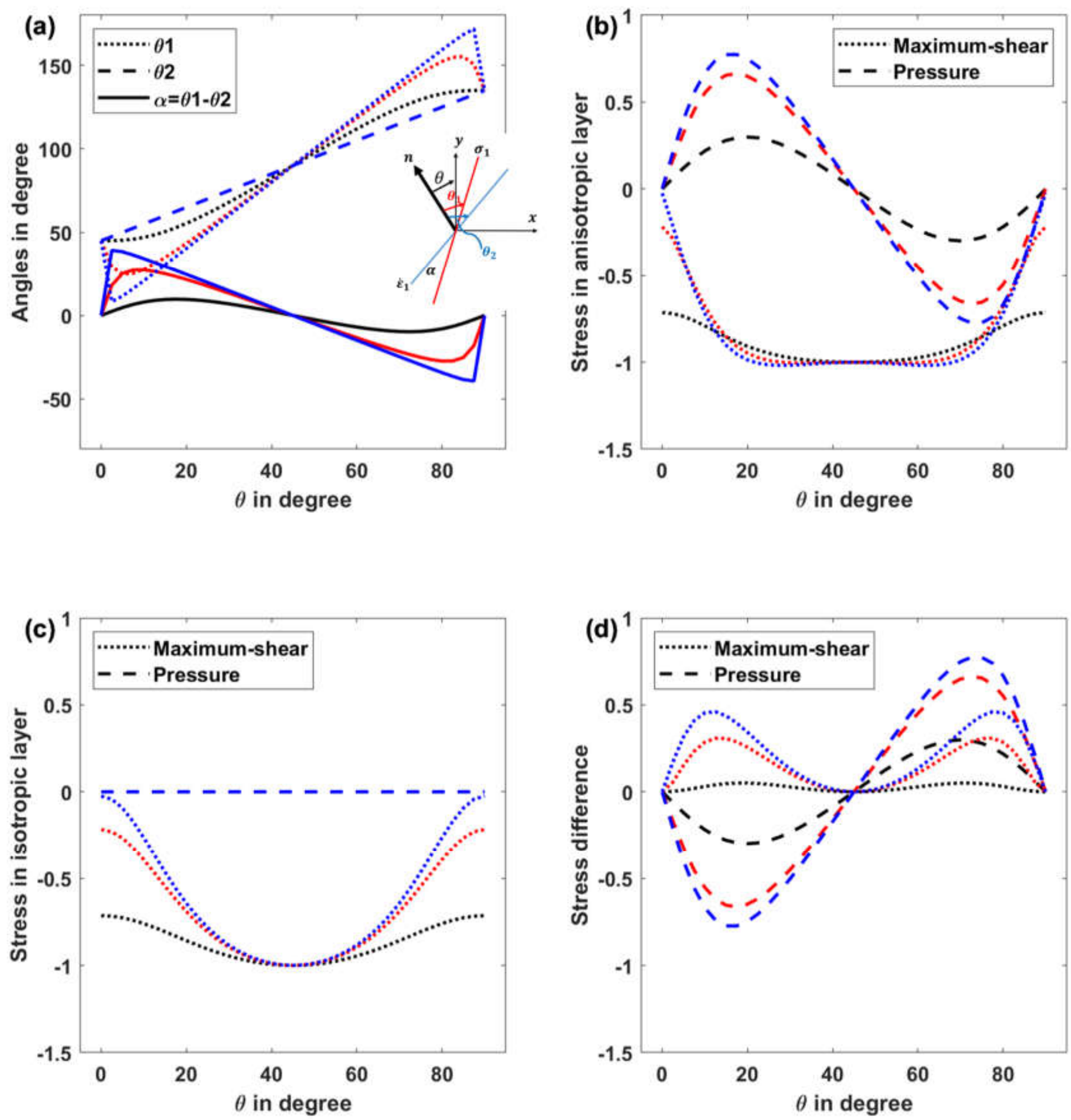

Figure 3. (a) Angular relations between principal stress σ_1, principal strain rate $\dot{\varepsilon}_1$, and the normal director $\boldsymbol{n}$ of the weak anisotropic viscosity, which are θ_1 and θ_2, respectively, for three viscosity contrasts $\gamma = 100$ (blue), $\gamma = 10$ (red), and $\gamma = 2$ (black) (b) Maximum shear stress and pressure as a function of θ at a point, $x = 0$, $y = -0.3$, inside the anisotropic layer. c) Maximum shear stress and pressure as a function of θ at $x = 0$, $y = -0.7$, inside the isotropic layer. (d) The difference of maximum shear stress and pressure between (b) and (c).

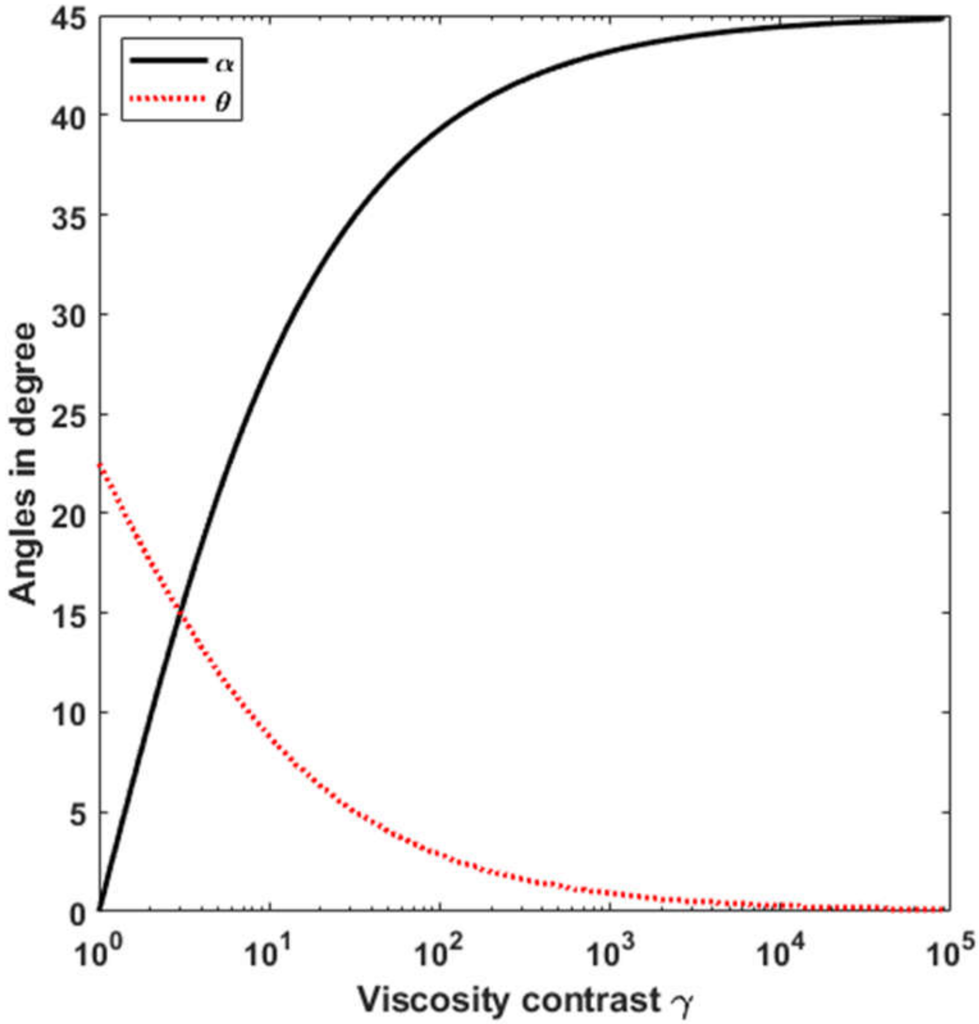

Figure 4. The peak angular mismatch α between principal stress σ_1 and principal strain rate $\dot{\varepsilon}_1$ as a function of viscosity contrast γ. For each γ, θ defines the normal vector of weak anisotropic direction at which the peak mismatch occurs. As γ increases, α increases and occurs at smaller θ.

Figures 3b and c show the maximum shear stress and pressure at a central point of the anisotropic layer ($x = 0$, $y = -0.3$) and the isotropic layer ($x = 0$, $y = -0.7$), respectively, for various θ and γ. Figure 3d shows the difference between Figures 3b and c. The heterogeneity of maximum shear stress and pressure show similar trends as to the mismatch α between the principal stress and strain rate axes while the peaks occur at larger θ. For example, the peak of maximum shear stress σ_{xy}^{max} is 0.05 when $\theta = 18.8°$ and $\gamma = 2$. σ_{xy}^{max} peaks at 0.31 when $\theta = 13.5°$ and $\gamma = 10$. σ_{xy}^{max} peaks at 0.46 when $\theta = 11.6°$ and $\gamma = 100$. The magnitudes of maximum shear stress and pressure heterogeneity may exert significant influence on the mechanical processes inside and outside of the viscously anisotropic zones.

3 Numerical solutions and 3-D problems

We confirmed that the results of section 2 were also reproduced by our earlier implementation of Moresi *et al.'s* (2003) approach into the *CitcomCU* (Moresi and Solomatov, 1995, Zhong *et al.*, 1998) and *CitcomS* (Zhong *et al.*, 2000, Tan *et al.*, 2006) convection codes (Becker and Kawakatsu, 2011), as was used by Ghosh *et al.* (2013).

However, for increased transparency, flexibility, and accessibility, and to be able to easily explore more complicated 2-D and 3-D scenarios, including for regional settings, we also developed a new finite-element code using the open-source computing platform *FEniCS* (Logg *et al.*, 2012, Logg and Wells, 2010) (https://fenicsproject.org/). This code can model 2-D and 3-D Stokes flow with viscous anisotropy and is available publicly via a *GitHub* repository (link provided in the Data and Software Availability Statement). We first verify the correctness of the code by modeling the same 2-D problem presented in section 2. Figure S1 in the supplementary material shows that the numerical solutions well match the analytical ones.

In *FEniCS*, the 2-D and 3-D codes share similar syntax with minimal changes. We use this tool to simulate 3-D models with more complexities. First, two simple theoretical models will be presented, then a more complex model inspired by the Leech River Schist above the Cascadia subduction zone (Bostock and Christensen, 2012 and references therein).

3.1 A conceptual model of major strike-slip fault zones

Figure 5a shows a 3-D model that is inspired by a major strike-slip fault zone, which is subjected to left lateral shearing. The fault zone is assumed mechanically anisotropic. The director of weak anisotropy, ***n***, is horizontal and is at an angle of θ relative to the y axis.

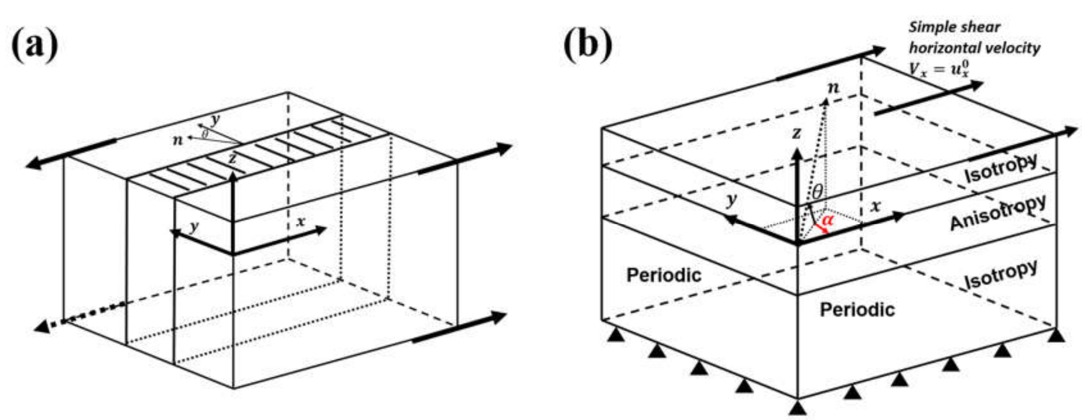

Figure 5. (a) Schematic of the 3-D model of a strike-slip fault zone. The fault zone is assumed mechanical anisotropic with the weak anisotropy direction $\boldsymbol{n}$. (b) Schematic diagram of the 3-D model of a horizontal anisotropic layer with the weak anisotropy direction $\boldsymbol{n}$.

The model is similar to the previous 2-D model except that a free surface is introduced. Figure 6 shows the results of a model with $\theta = 12.5°$, $\eta = 1$, $\gamma = 10$, and $v_x = \pm 1$. Horizontal velocity, pressure, and the 2nd invariant of stress tensor (a measure of the stress magnitude) on a horizontal and a vertical cross-section are shown. The principal stress (black) and strain rate (red) on the intersecting profile of the two cross-sections are projected to the *xz*, *yz*, and *xy* planes. We see distinct heterogeneity in pressure and the 2nd stress invariant inside the fault zone. From the map view (*xy* plane), axes of principal stress and strain rate are likewise mismatched inside the fault zone, as expected from section 2.

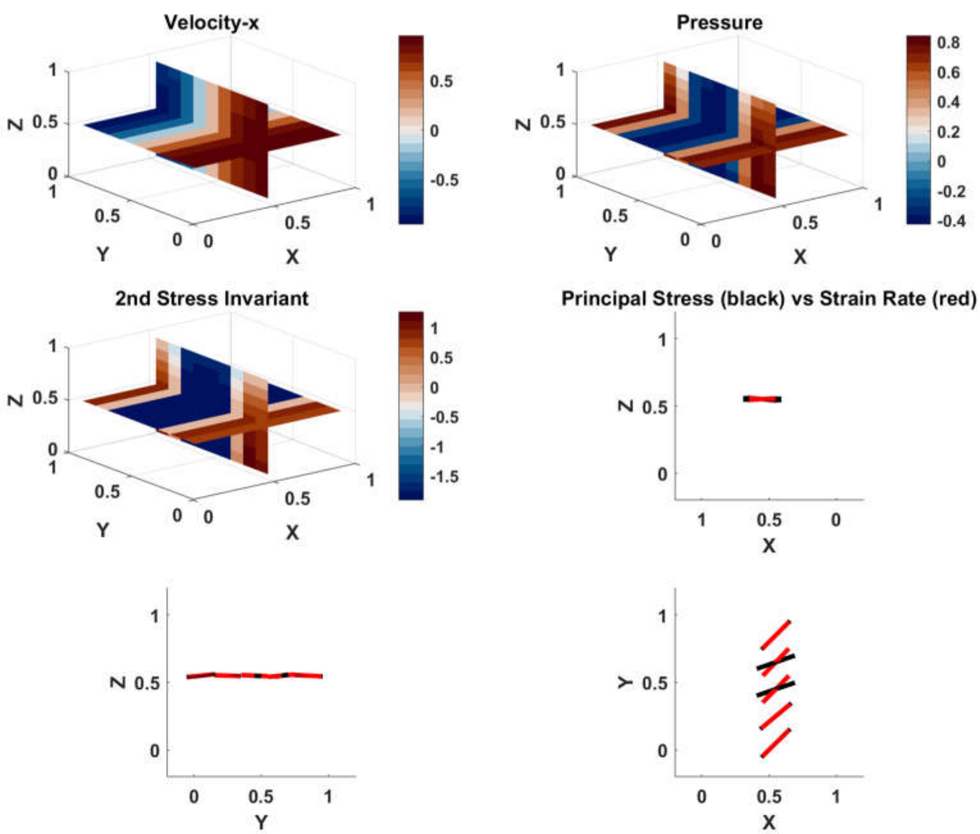

Figure 6. Numerical results on two cross-sections of horizontal velocity, pressure, and the 2nd invariant of stress tensor of the model in Figure 5a with the realization of $\theta = 12.5°$, $\eta = 1$, $\gamma = 10$, and $v_x = \pm 1$. Principal stress (black) and strain rate (red) on the intersecting profile of the two cross-sections are projected to the *xz*, *yz*, and *xy* planes.

3.2 A 3-D model for anisotropic asthenosphere of the upper mantle

Figure 5b shows a 3-D model with a horizontal anisotropic layer, which is conceptualized from the asthenosphere of the upper mantle (e.g., Becker and Kawakatsu, 2011). The model is more complicated than previous 2-D setup in terms of an additional angle α of the weak anisotropic director $\boldsymbol{n}$ relative to the vertical xz plane, as shown in Figure 5b (cf. Christensen, 1987).

We simulate a set of models with $\alpha = 45°$ and varying θ values. Figure 7 shows the results of a model with $\alpha = 45°$, $\theta = 10°$, $\eta = 1$, $\gamma = 10$, and $v_x^0 = 1$. Again, horizontal velocity, pressure, and the 2nd invariant of stress tensor on a horizontal and a vertical cross-section are shown. The principal stress (black) and strain rate (red) on the intersecting profile of the two cross-sections are projected to the xz, yz, and xy planes. We see clear heterogeneity in pressure and the 2nd stress invariant inside the anisotropic asthenosphere layer. Axes of principal stress and strain rate are mismatched in projections of all three orthogonal planes. The complexities increase compared to previous models as summarized in Table 1.

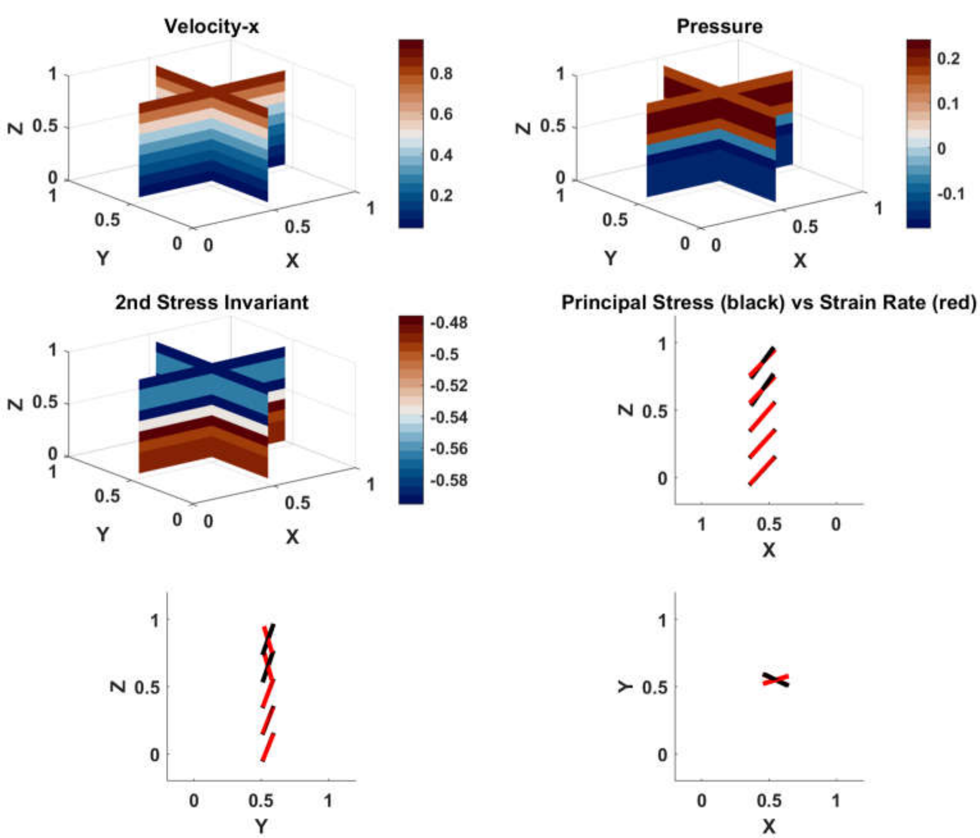

Figure 7. Numerical results on two cross-sections of horizontal velocity, pressure, and the 2nd invariant of stress tensor of the model in Figure 5b with the realization of $\alpha = 45°$, $\theta =$

$10°$, $\eta = 1$, $\gamma = 10$, and $v_x^0 = 1$. Principal stress (black) and strain rate (red) on the intersecting vertical profile of the two cross-sections are projected to the *xz*, *yz*, and *xy* planes.

Table 1. Summary of heterogeneity and stress and strain rate axes mismatch for different angle combinations for the model in Figure 5b.

θ	α	2nd invariant Heterogeneous?	Pressure Heterogeneity?	Stress vs. strain Mismatch
0	45	No	No	Yes
45	45	Yes	No	Yes
90	45	No	No	No
Other angles	45	Yes	Yes	Yes

3.3 Leech River Schist above the Cascadia subduction zone

We expect viscous anisotropy may arise from structural anisotropy like schist structures, which are generally exposed and associated with subduction zone environments (e.g., Chapman *et al.*, 2010, Bostock and Christensen, 2012, Chapman, 2016, Xia and Platt, 2017). It appears the schist may overlap on top of the subducting oceanic plate (Xia and Platt, 2017) as reconstructed geologically in the southern California case, though the schists were transferred to shallow depth in subsequent geologic episodes.

In Cascadia between southern Puget Sound and central Vancouver Island, the Leech River Schist (LRS), which is bounded by two north dipping thrusts forming a wedge (Bostock and Christensen, 2012 and references therein), is another example. The LRS rides on top of the subducting Juan de Fuca plate relative to North America. The schistosity is generally west-east and vertically dipping while the tectonic loading is N56E. Figure 8a shows a simple finite-element model and boundary conditions inspired by the LRS. Figure 8b shows the finite-element tetrahedral mesh generated by the open-source 3-D finite element mesh generator *Gmsh* (Geuzaine and Remacle, 2009) (https://gmsh.info/) as integrated with *FEniCS*.

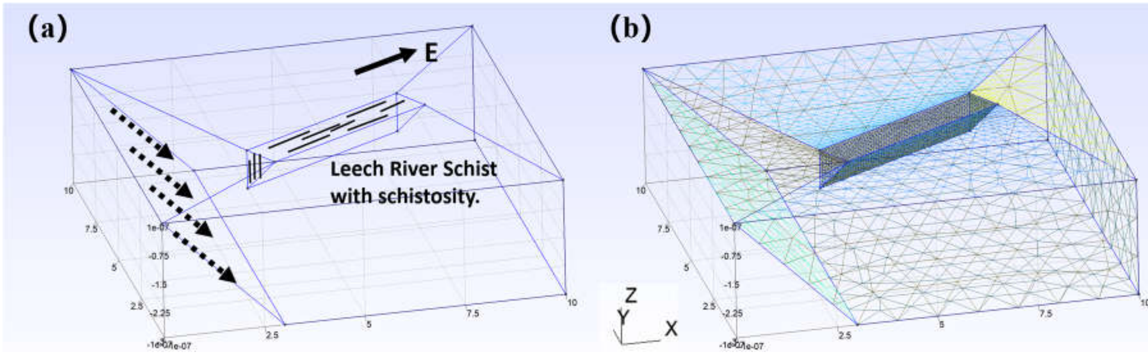

Figure 8. (a) Finite-element model of the Leech River Schist model. The schist is at the center of the model with west-east trending and vertically dipping schistosity. East is indicated. Dashed lines show the subducting of the Juan de Fuca plate. Except for the free surface, other boundaries are limited at zero normal velocities. (b) Tetrahedral finite-element mesh generated by the open-source mesh generator *Gmsh*.

Figure 9a-9c presents the axes of principal stress and strain rate on three orthogonal cross-sections - *xy* plane at z = -0.5, *yz* plane at x = 5, and *xz* plane at y = 5 - that cut through the schist, respectively. We see clearly that the map view (Figure 9a) and a side view (Figure 9b) reveal significant mismatch of axes of principal stress and strain rate inside the LRS.

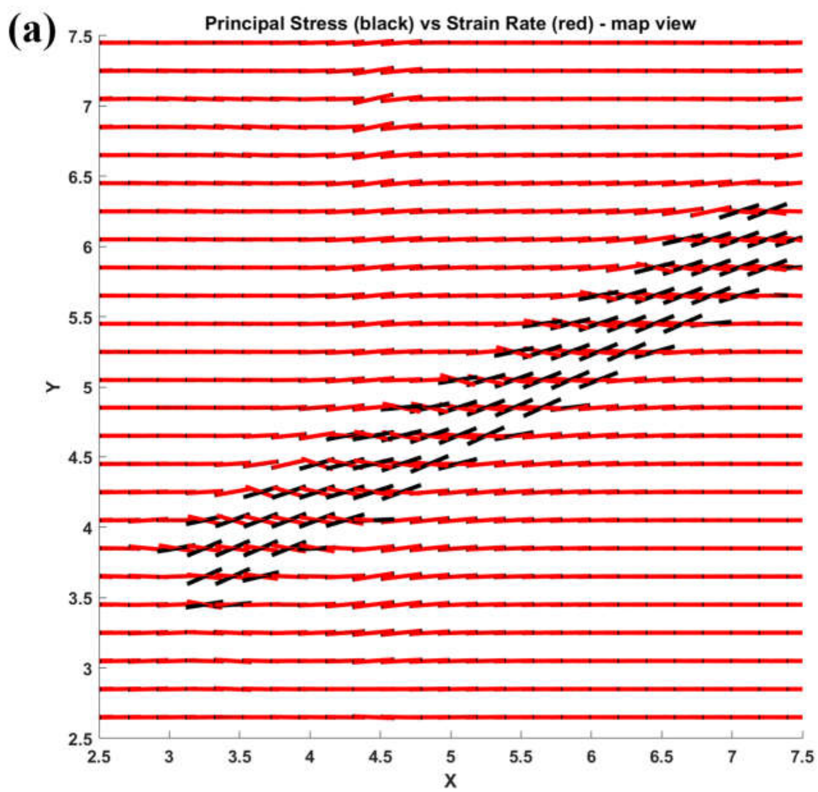

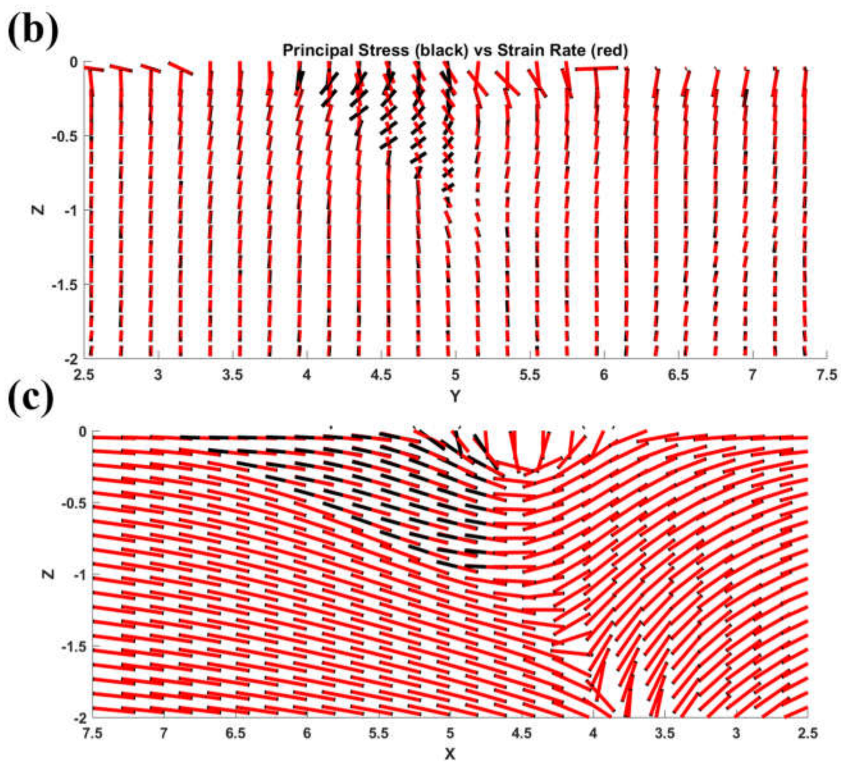

Figure 9. Principal stress (black bars) and principal strain rate (red bars) of a horizontal cross-section (a) at z = -0.5, of two vertical cross-sections (b) at x=5 and (c) at y =5 that cut through the Leech River Schist. Significant mismatch of principal stress and strain rate can be seen inside the schist wedge.

4. An approach to detect and constrain viscous anisotropy

Our results demonstrate that the existence of anisotropic structures can lead to significant non-coaxiality between principal stress and strain rate for plausible scenarios for viscous anisotropy, such as due to SPOs and CPOs (Mameri *et al.*, 2021). This motivates reassessment of measures for inferring stress or stressing-rates (e.g., Michael, 1984) and strain-rates derived from geodetic constraints (e.g., Smith-Konter and Sandwell, 2009). Close to faults in southern California, the two fields match in their alignment on broad scales, but there are also significant local deviations (Becker *et al.*, 2005; Yang and Hauksson, 2013) which are expected to be of relevance for long-term tectonics as well as setting local stress conditions for earthquake rupture.

Schulte-Pelkum *et al.* (2021) discussed a wider range of deformation indicators for southern California from the surface to the asthenosphere mantle. These authors found general consistency with N-S compression and E-W extension near the surface and in the asthenospheric mantle, but all lithospheric anisotropy indicators deviate from such patterns. One interpretation was deformation memory from the Farallon subduction and subsequent extension.

Notably, a comparison of focal mechanism-based principal stress axes (Yang and Hauksson, 2013) with GNSS-derived principal strain rates (Sandwell *et al.*, 2016) shows an angular mismatch with a peaked distribution centered on an azimuth (CW from N) of −6° with a standard deviation of 19°. Based on our results (Figure 3a), the observations may indicate mild mechanical anisotropy of viscosity contrast of 2…10 in the region for nearly all the θ if we assume the director of weak anisotropy were horizontal. The higher viscosity contrast of 100 is also possible if $20° < \theta < 70°$. We suggest further exploration of such observations with enhanced models and constraints, such as those recently provided by InSAR based deformation maps and smaller magnitude, better constrained focal mechanisms.

The non-coaxiality of principal stress and strain rate is more visible if the loading direction is misoriented from the weak anisotropic direction (cf. Ghosh *et al.*, 2013), such as for the settings explored in section 3. The case of Leech River Schist and the structure in southern California illustrate that the condition of misoriented loading and weak anisotropy (such as schistosity) may be common in nature. In addition to non-coaxial principal axes, significant heterogeneity of stress and pressure may occur as well.

For example, using teleseismic receiver functions, Audet (2015) finds that the plane of fast velocity strikes parallel to the San Andreas fault while dipping mildly throughout the crust near Parkfield. He interprets the mid-crustal anisotropy as fossilized fabric within fluid-rich foliated mica schists. Our results suggest that heterogeneity of stress and pressure might indeed be induced by the mechanical anisotropy of the schist, which could influence the stress distribution in the region and nearby earthquakes.

5. Conclusion

We present an analytical solution of a 2-D viscously anisotropic layer subjected to simple shearing which predicts significant stress heterogeneity and non-coaxial stress and strain rates. Observations of the non-coaxiality could give us constraints on the role of mechanical anisotropy in nature. Such analysis may be possible, e.g., by comparing stress inversions from focal mechanisms, surface strain rates from geodetic measurements, and integrated strain from seismic anisotropy (Schulte-Pelkum *et al.*, 2021).

To accelerate such studies, we develop an open-source finite-element code using *FEniCS*, verify the 2-D version of the code against the analytic solution, and explore a number of 3-D illustrative cases including a Leech River Schist above the Cascadia subduction zone scenario. We hope that this exploration of mechanical anisotropy for tectonic problems and our new implementation will help advance model and verification of mechanically anisotropic lithospheric models, and their implications, from long-term plate boundary evolution to fault loading and rupture propagation.

Acknowledgements

DL, SP, and TWB were partially funded by NSF EAR-2121666 and 1927216, and preliminary work was supported by the *Southern California Earthquake Center*

(Contribution No. 11877). SCEC is funded by NSF Cooperative Agreement EAR-1600087 & USGS Cooperative Agreement G17AC00047. LM was supported by the Australian Research Council Discovery Scheme, DP150102887.

Data and Software Availability Statement

The *FEniCS* codes, the *MATLAB* code for the analytical solution, and MATLAB post-processing scripts for the figures, simulation results, and documentation are hosted in the *GitHub* repository https://github.com/dunyuliu/Toolset_for_Mechanical_Anisotropy. (The repository is currently attached as a zip file for the review process, and it will be publicly available if the manuscript is accepted). *FEniCS* is available via https://fenicsproject.org/. We use the latest stable release of legacy FEniCS version 2019.1.0. *MATLAB* is available via https://www.mathworks.com/. Academic License is used in this work. *Gmsh* is available via https://gmsh.info/. Fabio Crameri's colormap is used (Crameri, 2018, Crameri, 2021).

References

Audet, P., 2015. Layered crustal anisotropy around the San Andreas Fault near Parkfield, California, *J Geophys Res-Sol Ea,* 120**,** 3527-3543.

Becker, T.W., Hardebeck, J.L. & Anderson, G., 2005. Constraints on fault slip rates of the southern California plate boundary from GPS velocity and stress inversions, *Geophys J Int,* 160**,** 634-650.

Becker, T.W. & Kawakatsu, H., 2011. On the role of anisotropic viscosity for plate-scale flow, *Geophysical Research Letters,* 38.

Becker, T.W. & Lebedev, S., 2021. *Dynamics of the Upper Mantle in Light of Seismic Anisotropy,* First edn, Vol., pp. Pages, John Wiley & Sons, Inc.

Bostock, M.G. & Christensen, N.I., 2012. Split from slip and schist: Crustal anisotropy beneath northern Cascadia from non-volcanic tremor, *J Geophys Res-Sol Ea,* 117.

Chapman, A.D., 2016. The Pelona–Orocopia–Rand and related schists of southern California: a review of the best-known archive of shallow subduction on the planet, *International Geology Review,* 59**,** 664-701.

Chapman, A.D., Kidder, S., Saleeby, J.B. & Ducea, M.N., 2010. Role of extrusion of the Rand and Sierra de Salinas schists in Late Cretaceous extension and rotation of the southern Sierra Nevada and vicinity, *Tectonics,* 29.

Christensen, U.R., 1987. Some Geodynamical Effects of Anisotropic Viscosity, *Geophys J Roy Astr S,* 91**,** 711-736.

Crameri, F., 2018. Geodynamic diagnostics, scientific visualisation and StagLab 3.0, *Geoscientific Model Development,* 11**,** 2541-2562.

Crameri, F., 2021. Scientific colour maps.

Geuzaine, C. & Remacle, J.F., 2009. Gmsh: A 3-D finite element mesh generator with built-in pre- and post-processing facilities, *Int J Numer Meth Eng,* 79**,** 1309-1331.

Ghosh, A., Becker, T.W. & Humphreys, E.D., 2013. Dynamics of the North American continent, *Geophys J Int,* 194**,** 651-669.

Hansen, L.N., Warren, J.M., Zimmerman, M.E. & Kohlstedt, D.L., 2016. Viscous anisotropy of textured olivine aggregates, Part 1: Measurement of the magnitude and evolution of anisotropy, *Earth and Planetary Science Letters,* 445**,** 92-103.

Hansen, L.N., Zimmerman, M.E. & Kohlstedt, D.L., 2012. Laboratory measurements of the viscous anisotropy of olivine aggregates, *Nature,* 492**,** 415-418.

Hardebeck, J.L. & Michael, A.J., 2004. Stress orientations at intermediate angles to the San Andreas Fault, California, *J Geophys Res-Sol Ea,* 109.

Hirano, S. & Yamashita, T., 2011. Analysis of the static stress field around faults lying along and intersecting a bimaterial interface, *Geophys J Int,* 187**,** 1460-1478.

Kaven, J.O., Maerten, F. & Pollard, D.D., 2011. Mechanical analysis of fault slip data: Implications for paleostress analysis, *J Struct Geol,* 33**,** 78-91.

Király, Á., Conrad, C.P. & Hansen, L.N., 2020. Evolving Viscous Anisotropy in the Upper Mantle and Its Geodynamic Implications, *Geochemistry, Geophysics, Geosystems,* 21**,** e2020GC009159.

Lev, E. & Hager, B.H., 2011. Anisotropic viscosity changes subduction zone thermal structure, *Geochem Geophy Geosy,* 12.

Long, M. and Becker. T.W., 2010. Mantle dynamics and seismic anisotropy, *Earth and Planetary Science Letters* 297, 341-354.

Logg, A. & Wells, G.N., 2010. DOLFIN: Automated Finite Element Computing, *Acm Transactions on Mathematical Software,* 37**,** Article 20.

Logg, A., Wells, G.N. & Hake, J., 2012. Chapter 10 DOLFIN: a C++/Python finite element library. *in Automated Solution of Differential Equations by the Finite Element Method*, pp. 173-225, eds. Logg, A., Mardal, K.-A. & Wells, G. Springer Berlin Heidelberg, Berlin, Heidelberg.

Mameri, L., Tommasi, A., Signorelli, J. & Hassani, R., 2021. Olivine-induced viscous anisotropy in fossil strike-slip mantle shear zones and associated strain localization in the crust, *Geophys J Int,* 224**,** 608-625.

Michael, A.J., 1984. Determination of Stress from Slip Data - Faults and Folds, *Journal of Geophysical Research,* 89**,** 1517-1526.

Montési, L.G.J., 2013. Fabric development as the key for forming ductile shear zones and enabling plate tectonics, *J Struct Geol,* 50**,** 254-266.

Moresi, L., Dufour, F. & Muhlhaus, H.B., 2003. A Lagrangian integration point finite element method for large deformation modeling of viscoelastic geomaterials, *J Comput Phys,* 184**,** 476-497.

Moresi, L. & Mühlhaus, H.B., 2006. Anisotropic viscous models of large-deformation Mohr–Coulomb failure, *Philosophical Magazine,* 86**,** 3287-3305.

Moresi, L.N. & Solomatov, V.S., 1995. Numerical Investigation of 2d Convection with Extremely Large Viscosity Variations, *Physics of Fluids,* 7**,** 2154-2162.

Mühlhaus, H.B., Moresi, L. & Cada, M., 2004. Emergent Anisotropy and Flow Alignment in Viscous Rock, *Pure and Applied Geophysics,* 161**,** 2451-2463.

Mühlhaus, H.B., Moresi, L., Hobbs, B. & Dufour, F., 2002. Large Amplitude Folding in Finely Layered Viscoelastic Rock Structures, *Pure and Applied Geophysics,* 159**,** 2311-2333.

Perry-Houts, J. & Karlstrom, L., 2019. Anisotropic viscosity and time-evolving lithospheric instabilities due to aligned igneous intrusions, *Geophys J Int,* 216**,** 794-802.

Sandwell, D.T., Zeng, Y., Shen, Z.-K., Crowell, B., Murray, J., McCaffrey, R. & Xu, X., 2016. The SCEC community geodetic model V1: Horizontal velocity grid. Tech. Rep. Scripps Institution of Oceanography, UCSD.

Schulte-Pelkum, V., Becker, T.W., Behr, W.M. & Miller, M.S., 2021. Tectonic Inheritance During Plate Boundary Evolution in Southern California Constrained From Seismic Anisotropy, *Geochem Geophy Geosy,* 22**,** e2021GC010099.

Simons, F.J. & van der Hilst, R.D., 2003. Seismic and mechanical anisotropy and the past and present deformation of the Australian lithosphere, *Earth and Planetary Science Letters,* 211**,** 271-286.

Smith-Konter, B. & Sandwell, D., 2009. Stress evolution of the San Andreas fault system: Recurrence interval versus locking depth, *Geophysical Research Letters,* 36.

Takei, Y. & Katz, R.F., 2013. Consequences of viscous anisotropy in a deforming, two-phase aggregate. Part 1. Governing equations and linearized analysis, *Journal of Fluid Mechanics,* 734**,** 424-455.

Tan, E., Choi, E., Thoutireddy, P., Gurnis, M. & Aivazis, M., 2006. GeoFramework: Coupling multiple models of mantle convection within a computational framework, *Geochem Geophy Geosy,* 7.

Tommasi, A., Knoll, M., Vauchez, A., Signorelli, J., Thoraval, C. & Loge, R., 2009. Structural reactivation in plate tectonics controlled by olivine crystal anisotropy, *Nat Geosci,* 2**,** 422-426.

Vauchez, A., Tommasi, A. & Barruol, G., 1998. Rheological heterogeneity, mechanical anisotropy and deformation of the continental lithosphere, *Tectonophysics,* 296**,** 61-86.

Xia, H. & Platt, J.P., 2017. Structural and rheological evolution of the Laramide subduction channel in southern California, *Solid Earth,* 8**,** 379-403.

Yang, W.Z. & Hauksson, E., 2013. The tectonic crustal stress field and style of faulting along the Pacific North America Plate boundary in Southern California, *Geophys J Int,* 194**,** 100-117.

Zhong, S.J., Gurnis, M. & Moresi, L., 1998. Role of faults, nonlinear rheology, and viscosity structure in generating plates from instantaneous mantle flow models, *J Geophys Res-Sol Ea,* 103**,** 15255-15268.

Zhong, S.J., Zuber, M.T., Moresi, L. & Gurnis, M., 2000. Role of temperature-dependent viscosity and surface plates in spherical shell models of mantle convection, *J Geophys Res-Sol Ea,* 105**,** 11063-11082.